RESEARCH ARTICLE

National Science Review
10: nwac234, 2023
https://doi.org/10.1093/nsr/nwac234
Advance access publication 22 October 2022

PHYSICS

High-efficiency nonlocal reflection-type vortex beam generation based on bound states in the continuum

Tongyu Li[1,†], Jiajun Wang[1,*,†], Wenjie Zhang[1,†], Xinhao Wang[1], Wenzhe Liu[2], Lei Shi[1,*] and Jian Zi[1,*]

ABSTRACT

Momentum-space polarization vortices centered at symmetry-protected bound states in the continuum of a periodic structure, e.g. photonic crystal slab, provide a novel nonlocal approach to generate vortex beams. This approach enjoys a great convenience of no precise alignment requirements, although the generation efficiency of the nonlocal generators requires further optimization before the practical application. In this work, we propose a temporal-coupled-mode-theory-based guideline for high-efficiency nonlocal reflection-type vortex generator design. The conversion efficiency of the vortex beam is found to be limited by the ratio of the radiative loss to the intrinsic absorption in practical systems. To increase this ratio through mode selection and structure design, the photonic crystal slabs are theoretically designed and experimentally characterized, showing a maximum on-resonance conversion efficiency of up to 86%. Combining high efficiency with simple fabrication and no requirement for precise alignment, reflection-type photonic crystal slabs could offer a new and competitive way to generate vortex beams flexibly.

Keywords: photonic crystal slab, vortex beam, bound states in the continuum

[1]State Key Laboratory of Surface Physics, Key Laboratory of Micro- and Nano-Photonic Structures (Ministry of Education) and Department of Physics, Fudan University, Shanghai 200433, China and [2]Department of Physics, The Hong Kong University of Science and Technology, Hong Kong, China

*__Corresponding authors__. E-mails: lshi@fudan.edu.cn; jjwang19@fudan.edu.cn; jzi@fudan.edu.cn
†Equally contributed to this work

Received 9 March 2022; **Revised** 15 September 2022; **Accepted** 25 September 2022

INTRODUCTION

The orbital angular momentum (OAM) of light is a new degree of freedom that can be used to modulate propagating lights [1,2]. The vortex beam (VB), as one of the carriers of OAM, features a spiral wave front and a central zero-intensity singularity [3,4]. Applications of VBs have been extensively investigated in imaging [5], optical manipulation [6–8] and optical communication [9] since VBs were first discovered in 1992 [10]. To implement these applications, VB generation has been realized over a wide wavelength range [11–17], with VBs mostly being generated using structures with an alignment center.

These conventional methods follow a similar intrinsic motivation to generate VBs, which involves the manipulation of incident beams using observable spiral or rotating structures in real space to form the spiral phase distributions. Among these methods, the most direct approach is to use a spiral phase plate that has a radially varying thickness to accumulate the spiral propagation phase for normally incident plane waves and was first realized at millimetre-wave frequency [18]. As a feasible method for use in the visible light range, the q-plate is an inhomogeneous half-wave plate made from liquid crystal that has a rotating in-plane optical axis orientation; the q-plate will add an additional spiral phase distribution to the normal incident beam, while also performing its polarization transformation function [19]. A programmable version has been derived based on the same generating principle in the form of a spatial light modulator [20–22]. Additionally, spiral wave fronts can also be recovered using fork-grating-shaped interference patterns recorded by holograms [23]. In recent years, a more compact and integrable method, called the metasurface [24], has been demonstrated to be capable of performing VB generation in the near infrared and visible light ranges using individually designed and fabricated units. However, all the generators mentioned above require the beam centers to be carefully aligned with their respective geometric centers. In the visible region, the resulting alignment difficulties become significant in practical applications.

Recently, a new nonlocal VB generation method based on the use of momentum-space polarization vortices centered at the symmetry-protected bound states in the continuum [25–29] of periodic structures was proposed [30]. These periodic structures, e.g. two-dimensional photonic crystal (PhC) slabs, can reduce difficulties caused by beam alignment and high-precision fabrication requirements in practical applications, although the low generation efficiency that occurs in conventional methods also occurs in this method.

RESULTS AND DISCUSSION

To improve VB generation efficiency, by intricately designing individual units at micro- or nanometer scale, metasurface generators have realized great progress [31,32]. Similar to the metasurface, the perfect mirror can also be introduced to block the transmission channels in nonlocal VB generation systems, which will then only transfer the incident energy to the reflection channel. We theoretically proposed that VB generation using single resonances and a perfect mirror in a reflection-type system can achieve 100% cross-polarized conversion efficiency [33]. However, when the practical applications at visible and near-infrared wavelengths are considered, the absorption of the metal mirror will inevitably cause a loss that will reduce the conversion efficiency of such a VB generator greatly. In this work, we propose a general picture based on temporal coupled mode theory (TCMT) [34] to improve the VB generation efficiency of reflection-type generators with intrinsic absorption, which is determined by the ratio of the radiative loss to the intrinsic absorption. Based on this picture, mode selection and structure design are employed to increase this ratio efficiently. In both simulations and experiments, the maximum on-resonance conversion efficiency of the designed reflection-type PhC VB generators reaches up to 86%. The VB profiles generated at different wavelengths and in different working regions are also observed experimentally.

To illustrate the mechanism of a nonlocal VB generator, considering a PhC slab for a particular frequency, a resonant mode, e.g. a guided resonance [35], above the light cone and below the diffraction limit will radiate into free space whose state of polarization (SOP) can therefore be defined in the far field. Close to the at-Γ bound state in the continuum (BIC), the SOPs of these guided resonances are nearly linearly polarized [36]. The major axes of these states rotate around the BIC singularity, driven by the rotational symmetry of the PhC slabs [30], forming strong polarization anisotropy in paraxial fields that leads to an extrinsic spin-orbit interaction [37–40]. When circularly polarized light impinges upon a PhC slab and interacts with these guided resonances around the BIC, the converted cross-polarized light will then gain Pancharatnam–Berry phases [41] and form a spiral wave front. The topological charge l of the spiral wave front is thus determined by the polarization charge q of the BIC, where $l = -2 \times q$ [30]. In addition, the polarization charge q of a BIC has been studied and has been shown to depend on the real space symmetry of the PhC slabs and the symmetry representation of the BIC mode [26,27].

For this generation principle, the VB generation efficiency is limited by the conversion efficiency of the resonance process. The topological charge l of the spiral wave front is thus determined by the polarization charge q of the BIC, where $l = -2 \times q$ [30]. In addition, the polarization charge q of a BIC has been studied and has been shown to depend on the real space symmetry of the PhC slabs and the symmetry representation of the BIC mode [26,27].

In TCMT, the dynamics of a resonance $A(\boldsymbol{k}_{||})$ on an isolated band [34] in a system with material absorption can be formulated as

$$\frac{\mathrm{d}A}{\mathrm{d}t} = \left(-i\omega_0 - \gamma_0 - \sum_{i=s,p}\gamma_i\right)A + \boldsymbol{K}^T|s_+\rangle, \tag{1}$$

$$|s_-\rangle = \boldsymbol{C}|s_+\rangle + \boldsymbol{D}A = \boldsymbol{S}|s_+\rangle. \tag{2}$$

Here, A is the amplitude of the resonance with eigenfrequency ω_0,γ_0 is the intrinsic loss due to material absorption and γ_i is the radiative loss. The column vectors $|s_+\rangle = (s_+, p_+)^T$ and $|s_-\rangle = (s_-, p_-)^T$ refer to the amplitudes of the incident and reflected light, respectively. We select the basis of s and p polarization to describe the system's two orthogonal energy ports to free space. The two-by-two matrix C provides the generalized background scattering matrix, with the two-by-two matrix $\boldsymbol{S}$ as the generalized scattering matrix. For a single resonance above the light cone and below the diffraction limit, the coupling matrices $\boldsymbol{K} = (k_s, k_p)^T$ and $\boldsymbol{D} = (d_s, d_p)^T$ are both two-by-one matrices. We can then certainly use the orthogonal coupling coefficients (d_s, d_p) to describe the SOP of the resonance[30].

Considering the energy conservation and time-reversal consideration, there are several constraints for the parameters above, which are written as

$$\boldsymbol{D}^\dagger\boldsymbol{D} = 2\gamma_i, \tag{3}$$

$$\boldsymbol{D} = \boldsymbol{K}, \tag{4}$$

$$\boldsymbol{C}\,\boldsymbol{D}^* = -\boldsymbol{D}. \tag{5}$$

Because of the fact that the SOPs of the resonances near the at-Γ bound states in the continuum are nearly linearly polarized [36], we then assume that the discussed resonance only coupled to the *s*-polarized port: $\gamma_i = \gamma_s$. Then, we obtain the results from the scattering matrix:

$$|d_s| = \sqrt{2\gamma_s}, \qquad |d_p| = 0, \tag{6}$$

$$\mathbf{S} = \begin{pmatrix} 1 - 2\gamma_s/[-i(\omega-\omega_0)+\gamma_0+\gamma_s] & 0 \\ 0 & 1 \end{pmatrix}$$

$$e^{i\phi} = \begin{pmatrix} s_{11} & 0 \\ 0 & 1 \end{pmatrix} e^{i\phi}. \tag{7}$$

We consider the resonances along the k_y-axis direction under near normal incidence to discuss their responses with different polarized incidences. In this case, the x (y) polarizations are nearly equivalent to the s (p) polarizations, with $d_x \approx d_s$, $d_y \approx d_p = 0$. The reflectance and absorptance that occur under x- (s-) and y- (p-)polarized incidence conditions are

$$R_s(\omega) = |s_{11}|^2, \tag{8}$$

$$A_s(\omega) = 1 - R_s(\omega) = \frac{4\gamma_0\gamma_s}{(\omega-\omega_0)^2 + (\gamma_0+\gamma_s)^2}. \tag{9}$$

Therefore, TCMT parameters (γ_s, γ_0 and ω_0) can then be obtained from reflectance spectra.

For a polarization vortex near the at-Γ BIC, the major axes of the SOPs would rotate around the Γ point. Considering a ψ angle between the major axes of the SOP and the x axes, similar conclusions are obtained via a rotational transformation of the axis. By transforming the basis from the s (p) basis $|s\rangle_{s,p}$ to the helical basis $|s\rangle_{l,r}$ [30], we can then describe the corresponding cases under circularly polarized incidence conditions:

$$\begin{aligned} |s_-\rangle_{l,r} &= \boldsymbol{T}_{helical}^{-1}\boldsymbol{R}^{-1}(\psi)\boldsymbol{S}\boldsymbol{T}_{helical}\boldsymbol{R}(\psi)|s_+\rangle_{l,r} \\ &= \frac{1}{2}\begin{pmatrix} s_{11}+1 & (s_{11}-1)e^{i2\psi} \\ (s_{11}-1)e^{-i2\psi} & s_{11}+1 \end{pmatrix}|s_+\rangle_{l,r}. \end{aligned} \tag{10}$$

If the incidence is circularly polarized, it can be found that the cross-polarized terms would gain a geometric phase [41] factor with different values of ψ, and the corresponding cross-polarized conversion efficiency is

$$R_c(\omega) = \left|\frac{s_{11}-1}{2}\right|^2 = \frac{\gamma_s^2}{(\omega-\omega_0)^2 + (\gamma_0+\gamma_s)^2}. \tag{11}$$

It is clearly shown here that the cross-polarized conversion efficiency will approach 100% on resonance when γ_0 vanishes. Practically, a reflection-type generator will still achieve a high conversion efficiency easily when $\gamma_s \gg \gamma_0$, as shown in the top left corner of Fig. 1(c). Because γ_0 relates to the intrinsic loss of the system and γ_s to the scattering of the guided resonance, mode selection and structure design are proposed to inhibit γ_0 and enlarge γ_s. For instance, as plotted in Fig. 1(b), the electric field of the first transverse-magnetic (TM)-like band is located on the mirror surface (see the online supplementary material), which leads to a large loss, while that of the second transverse-electric (TE)-like band approaches zero in the vicinity of the mirror, which leads to a smaller γ_0. With regard to γ_s, the radiative loss of the guided resonance corresponds to the light scattering caused by the periodic structures, for which the designed geometric parameters of the unit cells require further refinement.

To verify the above guideline, we designed reflection-type two-dimensional PhC slabs with the metallic mirror and characterized their conversion efficiencies both theoretically and experimentally. The studied reflection-type PhC slab consists of a flat silver mirror coated with an adhesion layer and a periodically etched Si_3N_4 dielectric layer. The silver mirror is formed by a 300-nm-thick film that was evaporated on a silicon substrate, above which a 25-nm-thick SiO_2 film was coated as an adhesion layer. The periodic structures are circular air hole arrays arranged in a square lattice with their fixed period of 460 nm; these structures were fabricated by electron beam lithography on dielectric layers.

To inhibit the γ_0 of the system, the TE_2 band was selected for the VB generation. As a VB generator, the momentum-space polarization field of the selected TE_2 band is shown in the online supplementary material, with the BIC being centered at the Γ point and the charge of the polarization vortex being +1. Considering the circularly polarized incidence, the cross-polarized light reflected via such a polarization vortex will gain a 4π spiral phase along any clockwise loop around the BIC singularity. As examples, the calculated phase distribution and the cross-polarized conversion efficiency iso-frequency contour of the TE_2 band were plotted in Fig. 2(a) and (b), respectively. To demonstrate the inhibition of γ_0, the electric field of the TE_2 band at $\boldsymbol{k}_{||}a/2\pi = (0.04, 0)$ is shown in Fig. 2(c). The electric field was demonstrated to gather sparingly above the silver film surface, indicating that only a small level of material absorption occurred in the system.

To enhance γ_s further in the selected TE_2 band, three geometrical parameters in the PhC slab required to be determined: the etched depth h, the

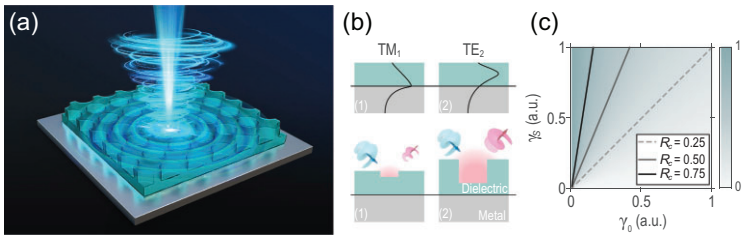

Figure 1. (a) Schematic view of the reflection-type PhC-VB generator. (b) In the top panel we plot the schematic electric field distributions of the TM_1 band and TE_2 band in the air-dielectric-metal structure. The field of TM_1 gathers on the surface of the metal mirror, causing large intrinsic absorption, i.e. $\gamma_0^{(1)} > \gamma_0^{(2)}$. Bottom panel: the large scattering rate caused by the geometric structure in a unit cell corresponds to large radiative loss, i.e. $\gamma_s^{(1)} < \gamma_s^{(2)}$. (c) Cross-polarized conversion efficiency R_c map calculated using (11) with normalized γ_0 and γ_s. Here R_c reaches high efficiency when $\gamma_s \gg \gamma_0$.

hole radius r and the dielectric layer thickness H. We focused on the conversion efficiency at $\boldsymbol{k}_{||}a/2\pi = (0.04, 0)$ on the iso-frequency contour to determine the parameters that provided high conversion efficiency. Starting with the PhC slab with parameters $h = 300$ nm, $r = 160$ nm and $H = 480$ nm, each of the parameters were varied within certain ranges to observe the variation in R_c. On the one hand, R_c at $\boldsymbol{k}_{||}a/2\pi = (0.04, 0)$ can be calculated with the different PhC parameters using rigorous coupled-wave analysis (RCWA) [42], as plotted with gray lines in Fig. 2(d). On the other hand, based on (11), the conversion efficiency was calculated using γ_0 and γ_s that can be extracted from the reflectance spectra (see the online supplementary material). The obtained γ_0 and γ_s values are depicted with light blue lines and the dark blue lines in Fig. 2(d), respectively. It was found that γ_0 is near zero, thus verifying the small level of absorption, and γ_s was strongly influenced by the structure. Using the extracted γ_0 and γ_s, the R_c spectra were then calculated using (11) and are indicated with green square markers in Fig. 2(d), which matched the simulated results well. With respect to the different selected parameters, R_c varied from 50% up to nearly 90% and remained higher than 80% over a wide parameter range, forming large flat steps in the middle of each panel. The high-efficiency flat step was also demonstrated experimentally and is shown in the online supplementary material.

By selecting a group of structural parameters on this flat step, i.e. $h = 337$ nm, $r = 186$ nm and $H = 519$ nm, the PhC slab was fabricated and characterized experimentally. As indicated by the polarization maps plotted in the online supplementary material, the proposed TE_2 band in the vicinity of the at-Γ BIC is only excited by *s*-polarized incident light along Γ-*X*, and the measured and calculated angle-resolved reflectance spectra under the *s*-polarized incidence along the Γ-*X* direction are illustrated in Fig. 3(a) and (b), respectively. The optical measurements were performed using our home-made angle-resolved imaging spectroscopy system [43–45], and the theoretical spectra were simulated via RCWA. The marked TE_2 band was used to generate the VB. The central frequency ω_0 and the corresponding γ_s and γ_0 values were extracted via numerically fitting the reflectance spectra at different wave vectors; examples are shown in Fig. 3(c). The cross-polarized conversion efficiency R_c in the experiments was obtained from the measured *s*-polarized reflectance spectra using (11). Obtained R_c values of the experimental TE_2 band at the different wavelengths are marked as green squares in Fig. 3(d), while the simulated R_c spectra along Γ-*X* under circularly polarized incidence are plotted as gray lines, showing high conversion efficiency over the entire TE_2 band and also showing good agreement with the theory; a detailed comparison is shown in the online supplementary material.

To further characterize the VB profiles, we built a home-made reflection-type Fourier-optics-based imaging system that had an imaging mode and an interferometer mode; a schematic diagram of this system is shown in Fig. 4(a). By taking the mirror in the reference path down, the system was firstly

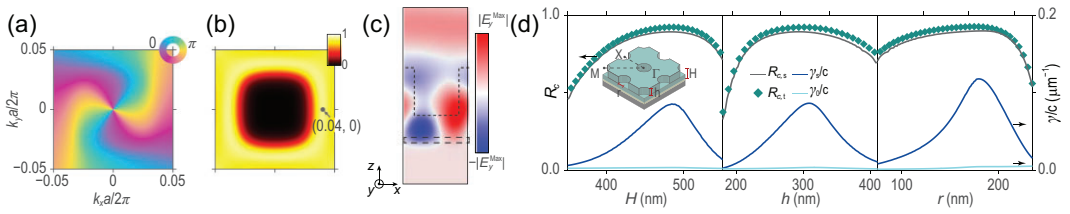

Figure 2. (a and b) The iso-frequency contour of phase and cross-polarized conversion efficiency at a wavelength of 797 nm under circular incidence ($h = 330$ nm, $r = 160$ nm and $H = 500$ nm). (c) Side view of the E_y distribution of band TE_2 at $\boldsymbol{k}_{||}a/2\pi = (0.04, 0)$. The dashed lines outline the PhC slab cross section in one unit cell. (d) The variation of R_c at $\boldsymbol{k}_{||}a/2\pi = (0.04, 0)$ on band TE_2 with different structure parameters. Gray lines represent simulated cross-polarized conversion efficiency, light blue lines and dark blue lines represent γ_s and γ_0 obtained from TCMT, and green squares represent calculated cross-polarized conversion efficiency from (11) using γ_s and γ_0. The schematic diagram of the PhC slab structure is shown in the inset; green part is an etched Si_3N_4 layer, yellow part is a SiO_2 film and gray part is a silver mirror.

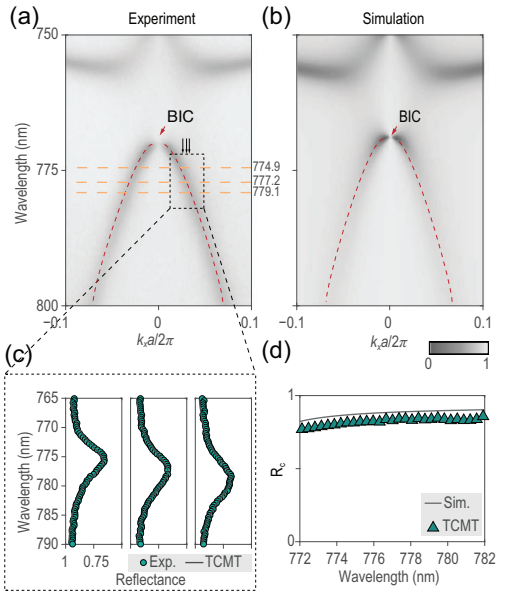

Figure 3. (a and b) The measured and simulated angle-resolved reflectance spectra along Γ-*X* under *s*-polarized incidence. Bands TE_2 were marked out by dashed lines. The vanishing point of band TE_2 corresponds to a central BIC. (c) Detailed experimental reflectance spectra at three different wave vectors, $\boldsymbol{k}_{||}a/2\pi = (0.027, 0)$, (0.031,0) and (0.034,0) (green dots), and corresponding fitting curves (gray lines) with TCMT. (d) The R_c obtained from measured band TE_2 at different wavelengths (green squares) whose maximum on-resonance conversion efficiency is 86%, and the simulated R_c spectra (gray line).

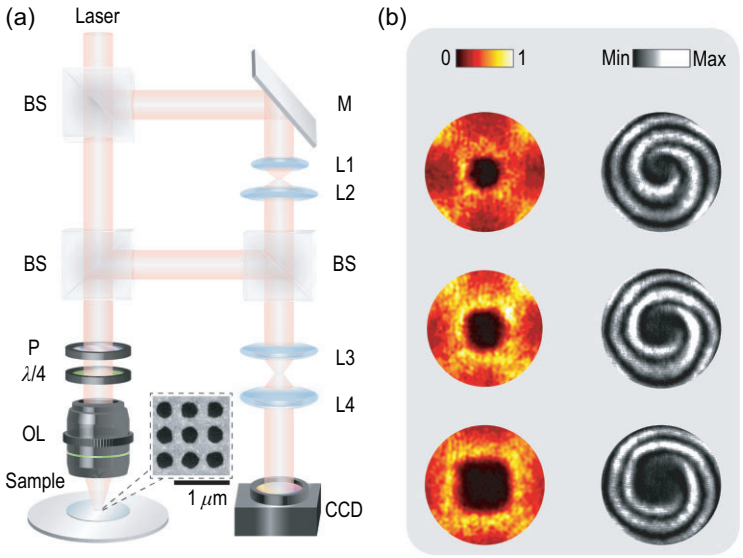

Figure 4. (a) The experimental setup. BS, beam splitter; L1–L4, lenses; M, mirror; OL, objective lens; P, polarizer; λ/4, 1/4 wave plate. Inset: the scanning electron microscope image of the PhC slab sample. (b) The measured results of fabricated PhC slabs. Left panel: the measured cross-polarized conversion efficiency. Right panel: the measured interference fringes between the generated spiral wave front and the reference wave front, where a singularity can be found in the center of the profile with 2 topological charge. From top to bottom, the wavelengths of incident LCP light were 774.9, 777.2 and 779.1 nm, respectively.

operated in imaging mode to measure the cross-polarized conversion efficiency iso-frequency contour, i.e. the beam profiles in the far field. In this mode, the reference light was not introduced into the measurement process. The incident laser was circularly polarized by a circular polarizer module (left-handed circularly polarized, or LCP) that included a linear polarizer and a 1/4 wave plate (1/4λ), and was then focused on our fabricated PhC slab through an objective lens (OL). The focused light impinged upon the PhC slab in all the directions allowed by the numerical aperture and was coupled with the *k*-variant guided resonances surrounding the BIC, causing the reflected light on these resonances to be strongly cross-polarized. Reversely passing through the same OL and circular polarizer module, the reflected light was then Fourier transformed into the momentum space. The beam profile was finally detected by a charge-coupled device (CCD) after imaging using a set of confocal lenses (L3 and L4). By varying the wavelength of the incident laser, beam profiles at 774.9, 777.2 and 779.1 nm, marked as orange dashed lines in Fig. 3(a), are plotted in the left panel in Fig. 4(b). It was observed that the generated beams had doughnut-shaped far-field profiles with central zero-intensity points, which is a key feature of VBs. Following the dispersion of the TE_2 band, the beam profile extended gradually in the momentum space and maintained high conversion efficiency.

Then, we switched on the mirror slightly to apply reference light for the operating interferometer mode. The linearly polarized reference light was used to illuminate the CCD to obtain interference patterns between the generated spiral wave front and the reference wave front. The interference patterns measured at the three wavelengths above are illustrated in the corresponding right panel of Fig. 4(b), where two obvious spiral arms can be observed at the profile center. This combination of a doughnut-shaped beam profile and the existence of spiral arms verified that the cross-polarized beam reflected by our fabricated PhC slab was a VB with a topological charge $l = -2$. Performing a Laguerre–Gaussian modal decomposition of the experimentally generated VB beam at 774.9 nm indicated that the energy of the $l = -2$ components accounted for 81.6% of the total energy of the generated beam, details of which are presented in the online supplementary material.

Furthermore, selecting three different regions on our fabricated PhC slab to perform the measurements, the beam profiles and the interference patterns were measured repeatedly with the incident light at 774.9 nm. The measurement regions are highlighted with red dots in the optical image shown in Fig. 5. By rotating the 1/4 wave plate, we demonstrated beam generation with both right-handed

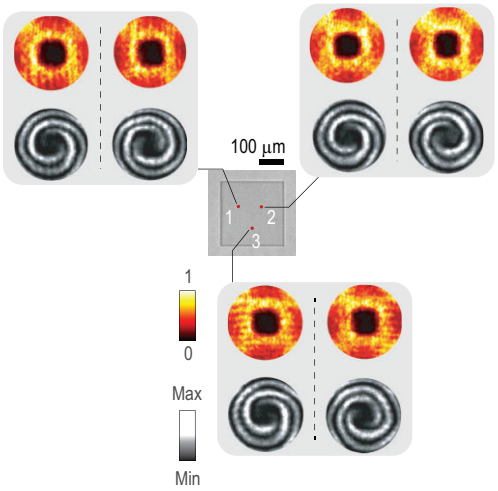

Figure 5. Inset: three measurement regions (red dots) on the optical image. The measured cross-polarized conversion efficiency and interference patterns in momentum space with LCP and RCP incidence respectively plotted in the left and right parts of the three gray panels.

circularly polarized (RCP) and LCP incidence. The beam profiles and the interference patterns remain unchanged, indicating that high-efficiency generation of the VB using a singularity in momentum space is nonlocal, i.e. it does not rely on the working position.

Here, we present some discussion. First, the nonlocal VB generation using our proposed principle is related to the at-Γ BIC, which can be realized flexibly at different wavelengths by tuning or even by simply scaling the structural parameters to make the band fall into the desired working region (see the online supplementary material). Additionally, we further make some comparison with some previous works that have made efforts to generate VBs via manipulations in momentum space. In these works, multiple-beam interference and spin-pseudospin coupling were used to selectively excite pseudospins located at K or K' valleys in artificial photonic graphene to generate VBs [46,47]. Note that these detected angular momentums did not result from the nonzero Berry curvature at the K and K' valleys, but instead resulted from the initial pseudospins of the Dirac system, while ours come from the polarization vortex existing around the at-Γ BIC. For practical applications, their methods may be suitable for generating VBs with oblique incidence, while our PhC-based methods are feasible with normal incidence.

CONCLUSIONS

In conclusion, we have reported a TCMT-based approach for the design of high-efficiency nonlocal reflection-type PhC slabs for VB generation. In this approach, selection of a particular working mode of the PhC slab can efficiently reduce the inevitable absorption loss of the metal mirror in both the visible and near-infrared wavelength ranges, and further structure design will boost the conversion efficiency. Using this approach, VBs can be efficiently generated using PhC slabs with no alignment centers and a simple fabrication process, bringing VBs one step closer to practical application use, such as optical communication, imaging and quantum information processing.

METHODS

Details are available in the online supplementary material.

SUPPLEMENTARY DATA

Supplementary data are available at *NSR* online.

FUNDING

This work was supported by the China National Key Basic Research Program (2022YFA1404800) and the National Natural Science Foundation of China (12234007 and 12221004). L.S. was further supported by the Science and Technology Commission of Shanghai Municipality (19XD1434600, 2019SHZDZX01, 19DZ2253000, 20501110500 and 21DZ1101500).

AUTHOR CONTRIBUTIONS

J.W., W.L., L.S., and J.Z. conceived the basic idea for this work. T.L. and J.W. designed the experiments. J.W. and X.W. fabricated PhC samples. W.Z. and J.W. developed the experimental setup. T.L., J.W. and W.Z. performed the optical experiments. L.S. and J.Z. supervised the research and the development of the manuscript. T.L. wrote the draft manuscript, and all authors took part in its revision and approved the final version.

Conflict of interest statement. None declared.

REFERENCES

1. Bliokh KY. Geometrical optics of beams with vortices: Berry phase and orbital angular momentum Hall effect. *Phys Rev Lett* 2006; **97**: 043901.
2. Dennis M, O'Holleran K and Padgett M. Singular optics: optical vortices and polarization singularities. In: Wolf E (ed) *Progress in Optics*, vol. **53**. Amsterdam: Elsevier, 2009, 293–363.
3. Ni J, Huang C and Zhou LM *et al.* Multidimensional phase singularities in nanophotonics. *Science* 2021; **374**: eabj0039.
4. Liu W, Liu W and Shi L *et al.* Topological polarization singularities in metaphotonics. *Nanophotonics* 2021; **10**: 1469–86.
5. Jack B, Leach J and Romero J *et al.* Holographic ghost imaging and the violation of a Bell inequality. *Phys Rev Lett* 2009; **103**: 083602.

6. Paterson L, MacDonald MP and Arlt J *et al.* Controlled rotation of optically trapped microscopic particles. *Science* 2001; **292**: 912–4.
7. Grier DG. A revolution in optical manipulation. *Nature* 2003; **424**: 810–6.
8. Padgett M and Bowman R. Tweezers with a twist. *Nat Photonics* 2011; **5**: 343–8.
9. Paterson C. Atmospheric turbulence and orbital angular momentum of single photons for optical communication. *Phys Rev Lett* 2005; **94**: 153901.
10. Allen L, Beijersbergen MW and Spreeuw R *et al.* Orbital angular momentum of light and the transformation of Laguerre-Gaussian laser modes. *Phys Rev A* 1992; **45**: 8185.
11. Mohammadi SM, Daldorff LK and Bergman JE *et al.* Orbital angular momentum in radio—a system study. *IEEE Trans Antennas Propag* 2009; **58**: 565–72.
12. Lin D, Fan P and Hasman E *et al.* Dielectric gradient metasurface optical elements. *Science* 2014; **345**: 298–302.
13. Miao P, Zhang Z and Sun J *et al.* Orbital angular momentum microlaser. *Science* 2016; **353**: 464–7.
14. Song D, Leykam D and Su J *et al.* Valley vortex states and degeneracy lifting via photonic higher-band excitation. *Phys Rev Lett* 2019; **122**: 123903.
15. Chen XD, Deng WM and Shi FL *et al.* Direct observation of corner states in second-order topological photonic crystal slabs. *Phys Rev Lett* 2019; **122**: 233902.
16. Gao X, Yang L and Lin H *et al.* Dirac-vortex topological cavities. *Nat Nanotechnol* 2020; **15**: 1012–8.
17. Huang C, Zhang C and Xiao S *et al.* Ultrafast control of vortex microlasers. *Science* 2020; **367**: 1018–21.
18. Turnbull G, Robertson D and Smith G *et al.* The generation of free-space Laguerre-Gaussian modes at millimetre-wave frequencies by use of a spiral phaseplate. *Opt Commun* 1996; **127**: 183–8.
19. Marrucci L, Manzo C and Paparo D. Optical spin-to-orbital angular momentum conversion in inhomogeneous anisotropic media. *Phys Rev Lett* 2006; **96**: 163905.
20. Cai X, Wang J and Strain MJ *et al.* Integrated compact optical vortex beam emitters. *Science* 2012; **338**: 363–6.
21. Genevet P, Lin J and Kats MA *et al.* Holographic detection of the orbital angular momentum of light with plasmonic photodiodes. *Nat Commun* 2012; **3**: 1278.
22. Liu S, Qi S and Zhang Y *et al.* Highly efficient generation of arbitrary vector beams with tunable polarization, phase, and amplitude. *Photonics Res* 2018; **6**: 228–33.
23. Mahmouli FE and Walker SD. 4-Gbps uncompressed video transmission over a 60-GHz orbital angular momentum wireless channel. *IEEE Wireless Commun Lett* 2013; **2**: 223–6.
24. Yu N and Capasso F. Flat optics with designer metasurfaces. *Nat Mater* 2014; **13**: 139–50.
25. Hsu CW, Zhen B and Lee J *et al.* Observation of trapped light within the radiation continuum. *Nature* 2013; **499**: 188–91.
26. Zhen B, Hsu CW and Lu L *et al.* Topological nature of optical bound states in the continuum. *Phys Rev Lett* 2014; **113**: 257401.
27. Zhang Y, Chen A and Liu W *et al.* Observation of polarization vortices in momentum space. *Phys Rev Lett* 2018; **120**: 186103.
28. Liu W, Wang B and Zhang Y *et al.* Circularly polarized states spawning from bound states in the continuum. *Phys Rev Lett* 2019; **123**: 116104.
29. Yoda T and Notomi M. Generation and annihilation of topologically protected bound states in the continuum and circularly polarized states by symmetry breaking. *Phys Rev Lett* 2020; **125**: 053902.
30. Wang B, Liu W and Zhao M *et al.* Generating optical vortex beams by momentum-space polarization vortices centred at bound states in the continuum. *Nat Photonics* 2020; **14**: 623–8.
31. Wang H, Li Y and Han Y *et al.* Vortex beam generated by circular-polarized metasurface reflector antenna. *J Phys D* 2019; **52**: 255306.
32. Akram MR, Bai X and Jin R *et al.* Photon spin Hall effect-based ultra-thin transmissive metasurface for efficient generation of OAM waves. *IEEE Trans Antennas Propag* 2019; **67**: 4650–8.
33. ,Liu W, Shi L and Zi J *et al.* Ways to achieve efficient non-local vortex beam generation. *Nanophotonics* 2021; **10**: 4297–304.
34. Fan S, Suh W and Joannopoulos JD. Temporal coupled-mode theory for the Fano resonance in optical resonators. *J Opt Soc Am A* 2003; **20**: 569–72.
35. Fan S and Joannopoulos JD. Analysis of guided resonances in photonic crystal slabs. *Phys Rev B* 2002; **65**: 235112.
36. Hsu CW, Zhen B and Soljačić M *et al.* Polarization state of radiation from a photonic crystal slab, arXiv, 2017. https://arxiv.org/abs/1708.02197.
37. Adachi H, Akahoshi S and Miyakawa K. Orbital motion of spherical microparticles trapped in diffraction patterns of circularly polarized light. *Phys Rev A* 2007; **75**: 063409.
38. Zhao Y, Edgar JS and Jeffries GD *et al.* Spin-to-orbital angular momentum conversion in a strongly focused optical beam. *Phys Rev Lett* 2007; **99**: 073901.
39. Bliokh KY, Rodríguez-Fortuño FJ and Nori F *et al.* Spin–orbit interactions of light. *Nat Photonics* 2015; **9**: 796–808.
40. Tang Y, Li K and Zhang X *et al.* Harmonic spin–orbit angular momentum cascade in nonlinear optical crystals. *Nat Photonics* 2020; **14**: 658–62.
41. Berry MV. The adiabatic phase and pancharatnam's phase for polarized light. *J Mod Opt* 1987; **34**: 1401–7.
42. Liu V and Fan S. S4: a free electromagnetic solver for layered periodic structures. *Comput Phys Commun* 2012; **183**: 2233–44.
43. Zhang Y, Zhao M and Wang J *et al.* Momentum-space imaging spectroscopy for the study of nanophotonic materials. *Sci Bull* 2021; **66**: 824–38.
44. Li T, Chen A and Fan L *et al.* Photonic-dispersion neural networks for inverse scattering problems. *Light Sci Appl* 2021; **10**: 154.
45. Wang J, Zhao M and Liu W *et al.* Shifting beams at normal incidence via controlling momentum-space geometric phases. *Nat Commun* 2021; **12**: 6046.
46. Song D, Paltoglou V and Liu S *et al.* Unveiling pseudospin and angular momentum in photonic graphene. *Nat Commun* 2015; **6**: 6272.
47. Liu JL, Ye WM and Zhang S. Pseudospin-induced chirality with staggered optical graphene. *Light Sci Appl* 2016; **5**: e16094.